ACS APPLIED MATERIALS & INTERFACES
Research Article
Cite This: ACS Appl. Mater. Interfaces 2018, 10, 13491−13498
www.acsami.org

Investigation of the Na Storage Property of One-Dimensional $Cu_{2-x}Se$ Nanorods

He Li,[†,§] Jiali Jiang,[†,§] Jianxing Huang,[†] Yunhui Wang,[†] Yueying Peng,[†] Yiyong Zhang,[†] Bing-Joe Hwang,[‡] and Jinbao Zhao*,[†]

[†] State Key Laboratory of Physical Chemistry of Solid Surfaces, Collaborative Innovation Center of Chemistry for Energy Materials, State-Province Joint Engineering Laboratory of Power Source Technology for New Energy Vehicle, College of Chemistry and Chemical Engineering, Xiamen University, Xiamen 361005, P. R. China

[‡] NanoElectrochemistry Laboratory, Department of Chemical Engineering, National Taiwan University of Science and Technology, Taipei 106, Taiwan

Supporting Information

ABSTRACT: In this study, one-dimensional $Cu_{2-x}Se$ nanorods synthesized by a simple water evaporation-induced self-assembly approach are served as the anode material for Na-ion batteries for the first time. $Cu_{2-x}Se$ electrodes express outstanding electrochemical properties. The initial discharge capacity is 149.3 mA h g^{-1} at a current density of 100 mA g^{-1}, and the discharge capacity can remain at 106.2 mA h g^{-1} after 400 cycles. Even at a high current density of 2000 mA g^{-1}, the discharge capacity of the $Cu_{2-x}Se$ electrode still remains at 62.8 mA h g^{-1}, showing excellent rate performance. Owing to the excellent electronic conductivity and one-dimensional structure of $Cu_{2-x}Se$, the $Cu_{2-x}Se$ electrodes manifest fast Na^+ ion diffusion rate. Moreover, detailed Na^+ insertion/extraction mechanism is further investigated by ex situ measurements and theoretical calculations.

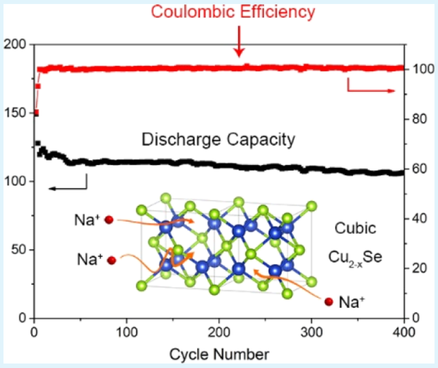

KEYWORDS: *copper selenide, Na-ion battery, Na storage property, intercalation mechanism, electrochemical kinetics*

INTRODUCTION

Li-ion batteries (LIBs) have been proved to be the most successful rechargeable battery system in the past two decades owing to their high energy density, high voltage, outstanding cyclic stability, and no memory effect. However, with the mounting demand of LIBs in portable electronic devices, electric vehicles, and grid-scale energy storage systems, there are growing concerns about the reserves and costs of lithium.[1−4] Alternatively, rechargeable non-LIBs such as Na-ion batteries (NIBs), K-ion batteries, Mg-ion batteries, and Al-ion batteries have attracted widespread concern in recent years.[5−8] Noticeably, much effort has been put into the investigation of NIBs, mainly because sodium shows physicochemical properties similar to those of lithium as they are both alkali metals. Moreover, sodium owns the advantages of low cost, rich reserves, and unrestricted distribution.[9−12] Nevertheless, most anode materials of NIBs (such as hard carbon and metal oxide) suffer from low energy density and inferior cyclic stability, attributed to larger relative atomic mass of Na and bigger radius of Na^+ ions.[13−15] Consequently, an ideal anode material should have a stable structure to accommodate Na^+ ions intercalating/extracting back and forth, with high specific capacity, long cycle life, and low cost.

Transition-metal chalcogenides have been intensively investigated as anode materials for LIBs and NIBs by virtue of their low price and high theoretical capacity.[16−23] Among them, $Cu_{2-x}Se$ possesses many unique physiochemical properties, which make it an ideal electrode material for NIBs. First, Se atoms of $Cu_{2-x}Se$ are located in face-centered cubic positions, whereas superionic Cu ions are kinetically disordered in this structure; thus, $Cu_{2-x}Se$ is a p-type conductor with ultrahigh electronic conductivity, which could be a prospective electrode material with outstanding rate performance.[24,25] Second, the cell volume of $Cu_{2-x}Se$ (195.32 $Å^3$) is much larger than that of copper sulfides with a similar crystal structure (171.23 $Å^3$).[26] A larger unit cell can better accommodate Na^+ ions inserting into the crystal cell, leading to better cycling performance and higher ionic diffusion rate.[24] Third, copper and selenium are widely dispersed in the earth's crust and their price is low.[22] Overall, $Cu_{2-x}Se$ can be a promising anode material candidate for NIBs.

Herein, one-dimensional $Cu_{2-x}Se$ nanorods are successfully synthesized via a facile water evaporation-induced self-assembly method. Thin $Cu_{2-x}Se$ nanowires are formed first and then bind together into bundles with diameters of 300−800 nm and lengths up to dozens of micrometers. Upon adjusting the cutoff voltage to 1.0−3.0 V, $Cu_{2-x}Se$ electrodes manifest outstanding electrochemical performance. The initial discharge capacity is

Received: January 15, 2018
Accepted: April 4, 2018
Published: April 4, 2018

DOI: 10.1021/acsami.8b00783

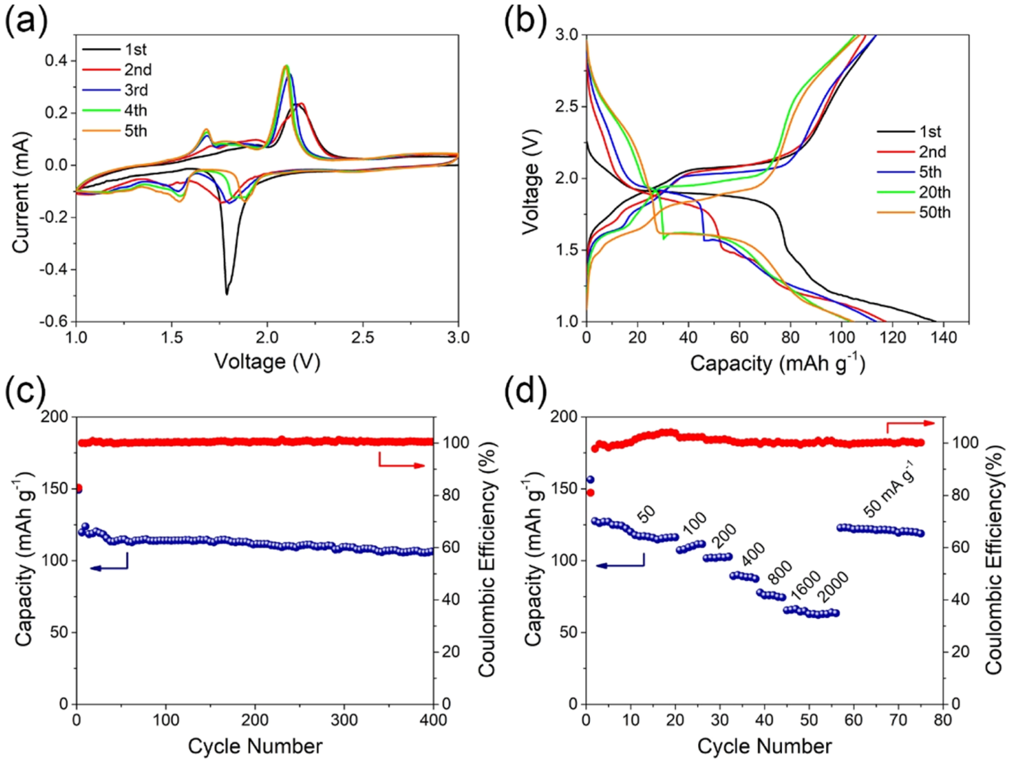

Figure 1. (a) Cyclic voltammograms of the $Cu_{2-x}Se$/Na battery at a scan rate of 0.2 mV s^{-1} in the voltage range of 1.0−3.0 V. (b) First, 2nd, 5th, 20th, and 50th galvanostatic discharge/charge curves of the $Cu_{2-x}Se$ electrodes at a current density of 100 mA g^{-1} in the potential range of 1.0 and 3.0 V versus Na^+/Na. (c) Cycling performance of the $Cu_{2-x}Se$/Na battery at a current density of 100 mA g^{-1}. (d) Rate performance of $Cu_{2-x}Se$ electrodes at different current densities.

149.3 mA h g^{-1} with a Coulombic efficiency of 82.9%. After 400 galvanostatic charge−discharge cycles, the specific discharge capacity remains at 106.2 mA h g^{-1}. A remarkable rate performance can also be observed; the discharge capacities of the $Cu_{2-x}Se$ electrodes are 124.7, 111.4, 102.2, 88.5, 75.9, 65.2, and 62.8 mA h g^{-1} at current densities of 50, 100, 200, 400, 800, 1600, and 2000 mA g^{-1}, respectively. In addition, the $Cu_{2-x}Se$ electrodes exhibit excellent electrochemical kinetics, which are explored by cyclic voltammetry (CV) and galvanostatic intermittent titration technique (GITT) tests. The diffusion coefficient is calculated to be up to 7.22×10^{-10} cm^2 s^{-1}. Moreover, ex situ X-ray diffraction (XRD) measurements, transmission electron microscopy (TEM) test, X-ray photoelectron spectroscopy (XPS) spectra, and Raman spectra are characterized to investigate the detailed insertion and extraction of Na into the framework of $Cu_{2-x}Se$, which can enrich the understanding of the electrochemical reaction mechanism of metal chalcogenides in NIBs.

■ RESULTS AND DISCUSSION

Phase and Morphology Characterization. One-dimensional $Cu_{2-x}Se$ nanorods were synthesized by a one-step and cost-effective water evaporation method, which was reported by our group and Xu et al. before.[27,28] The growth of $Cu_{2-x}Se$ nanorods can be found in Figures S1−S3 (Supporting Information), indicating the growth of $Cu_{2-x}Se$ along the (111) orientation. The XRD pattern and structural model of the as-prepared product are shown in Figure S4. The XRD pattern matches well with cubic $Cu_{2-x}Se$ [space group: $F\bar{4}3m$, powder diffraction card (PDF) no. 06-0680, Joint Committee on Powder Diffraction Standards (JCPDS), 2004] perfectly, suggesting the successful preparation of $Cu_{2-x}Se$ powder. The Raman spectrum of the synthesized product is shown in Figure S5. A strong band appears at 256 cm^{-1}, which can be assigned to the stretching vibration of the Se−Se bond. The weak band at 512 cm^{-1} corresponds with the first overtone of the strong band at 256 cm^{-1}.[29,30]

The scanning electron microscopy (SEM) and TEM images of as-prepared $Cu_{2-x}Se$ were obtained and are revealed in Figure S6, indicating that $Cu_{2-x}Se$ shows a rodlike morphology and the $Cu_{2-x}Se$ nanorods are crystalline. The energy-dispersive X-ray spectroscopy (EDS) spectrum of $Cu_{2-x}Se$ rods is presented in Figure S7. Several peaks ascribed to Cu Lα (0.930 keV), Se Lα (1.379 keV), Cu Kα (8.040 keV), and Se Kα (11.207 keV) confirm the existence of Cu and Se. According to the calculation, the atomic ratio of Cu:Se is 1.84; thus, the x value is determined to be 0.16.

Electrochemical Performance. The electrochemical tests were all performed in the voltage range of 1.0−3.0 V, which was optimized by adjusting the cutoff voltage of $Cu_{2-x}Se$/Na batteries (the detailed discussion can be found in Figure S8). The CV curves of the $Cu_{2-x}Se$/Na battery are presented in Figure 1a. In the first cathodic scan, a sharp reduction peak at 1.79 V can be assigned to the insertion of Na^+ ions into crystal cells of $Cu_{2-x}Se$. In the following cathodic scans, the reduction peak gradually separates into two peaks at around 1.85 and 1.53 V, which may represent two kinds of Na^+ ion intercalation positions, corresponding to defects of copper ions in the $Cu_{2-x}Se$ crystal structure and body-centered vacant positions of $Cu_{2-x}Se$ crystal cells, respectively. In the first anodic scan, an oxidation peak at 2.15 V suggests the extraction of Na^+ ions. In the subsequent anodic scans, the oxidation peak also separates into two peaks at around 2.10 and 1.68 V, which also

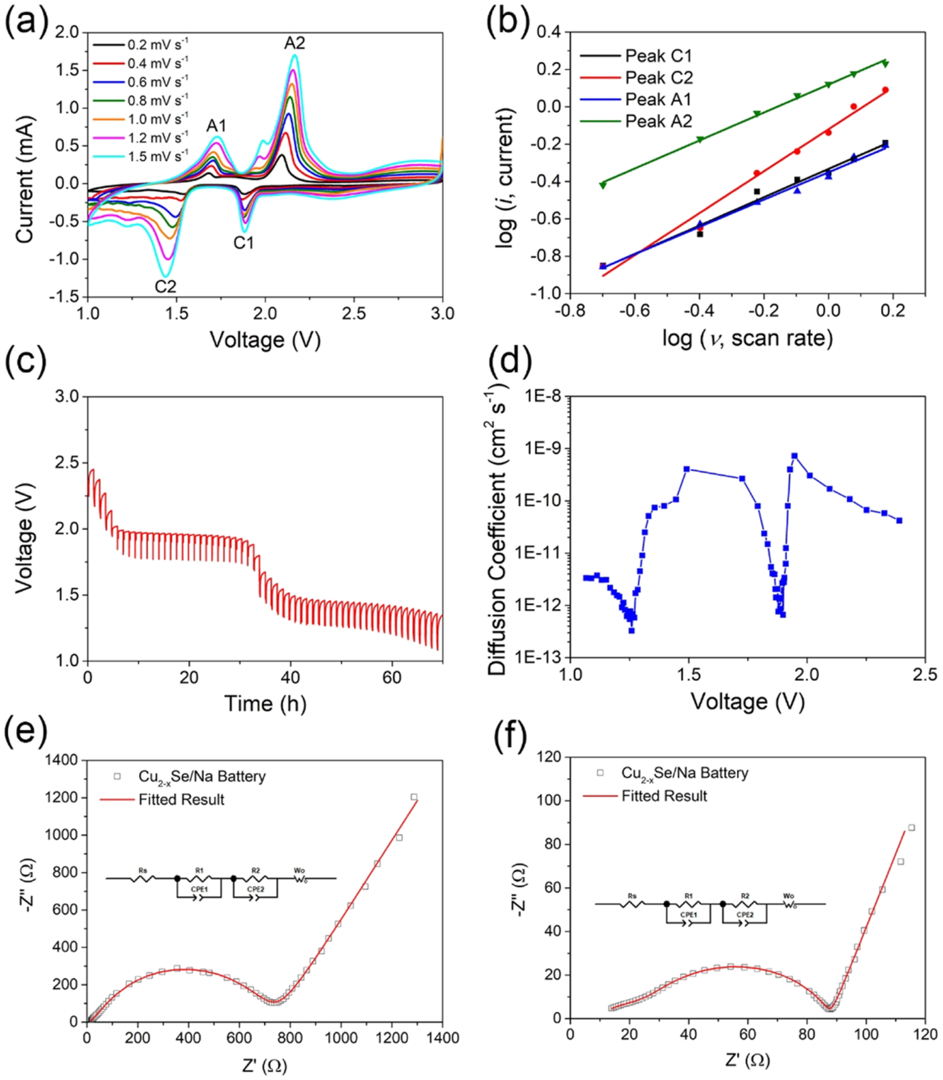

Figure 2. Kinetics characterization of $Cu_{2-x}Se$/Na batteries. (a) Cyclic voltammogram curves of the $Cu_{2-x}Se$/Na battery cycled 100 times at different sweep rates between 1.0 and 3.0 V. (b) Fitted lines of log(i) and log(ν). (c) GITT curve of the $Cu_{2-x}Se$/Na battery during the initial discharge process. (d) Diffusion coefficients of the $Cu_{2-x}Se$/Na battery calculated based on the GITT test. Nyquist plots of the $Cu_{2-x}Se$/Na battery (e) before electrochemical test and (f) after 20 charge−discharge cycles.

correspond to two extraction steps of Na^+ ions. The CV curves overlap well after the initial sweep, indicating the excellent electrochemical reversibility. The polarization has reduced slightly from the first to the fifth cycle, which can be attributed to the electrochemical activation of the $Cu_{2-x}Se$ electrode. As the CV test is in process, the electrolyte would infiltrate in the electrode gradually. In this way, the active material can contact the electrolyte better, and then the average Na^+ ion diffusion path can be shortened, leading to faster ionic diffusion rate and reduced polarization.

Figure 1b presents the 1st, 2nd, 5th, 20th, and 50th charge−discharge curves of the $Cu_{2-x}Se$/Na battery. In the initial discharge process, there is only an apparent plateau at around 1.9 V. We suppose that Na^+ ions mainly insert into the face-centered position (site a in Figure 4) because the insertion of Na^+ ions into site a is easier when site a and b are not occupied by Na^+ ions (Table 2). However, the extraction of Na^+ ions from site a is harder; not all Na^+ ions can be extracted from site a. In this way, this plateau shrinks and another plateau corresponding with the insertion of Na^+ ions into site b appears and extends in the following cycles. In the initial charge process, a plateau emerges at around 2.10 V, the plateau gradually goes to lower potential, and a short plateau at around 1.60 V appears in the following cycles, which is in accordance with the discharge process. The capacity−voltage curves are consistent with the CV curves. Additionally, the polarization of the $Cu_{2-x}Se$/Na battery decreases from the 1st cycle to the 50th cycle. This can be attributed to the electrochemical activation of the $Cu_{2-x}Se$ electrode.

The cycling performance of the $Cu_{2-x}Se$/Na battery at a current density of 100 mA g^{-1} is demonstrated in Figure 1c. The initial discharge capacity is 149.3 mA h g^{-1} with a Coulombic efficiency of 82.9%. The Coulombic efficiency of the first cycle is relatively higher than that of other metal chalcogenides such as CuS (80.5%) and Co_9S_8 (68.9%).[31,32] After 400 cycles, the discharge capacity remains at 106.2 mA h g^{-1} and the capacity retention rate is 83.0%, showing the outstanding cyclic stability. The capacity−voltage curves of the $Cu_{2-x}Se$/Na battery at different current densities are shown in Figure 1d. The battery capacity can stand at 124.7, 111.4, 102.2, 88.5, 75.9, 65.2, and 62.8 mA h g^{-1} at the current densities of 50, 100, 200, 400, 800, 1600, and 2000 mA g^{-1}, respectively.

When the current density drops to 50 mA g^{-1} again, the capacity can bounce to 122.0 mA h g^{-1}, showing good rate performance at high current density. Overall, the $Cu_{2-x}Se$ electrode manifests outstanding cyclic stability and good rate performance and hence can be a promising anode material for NIBs.

CV test at different scan rates, GITT test, and electrochemical impedance spectroscopy (EIS) were carried out to research the electrochemical kinetics of $Cu_{2-x}Se$/Na batteries. Figure 2a displays the CV curves at different scan rates; reduction peaks shift to lower potential and oxidation peaks shift to higher potential as the scan rate increases, which can be ascribed to the increased polarization of the $Cu_{2-x}Se$/Na battery. The peak current increases disproportionally to the square root of scan rate, indicating that the charge and discharge processes may comprise both faradic and non-faradic behaviors.[33,34] Equations 1 and 2 can describe the relationship between peak current (i) and scan rate (ν).

$$i = a\nu b \tag{1}$$

$$\log(i) = b\log(\nu) + \log(a) \tag{2}$$

where i is the current, ν is the scan rate, and a and b are relevant parameters. When b = 0.5, the electrochemical process is controlled by the ionic diffusion, whereas when b = 1, it is controlled by the pseudocapacitive behavior.[35] The fitted relationships of log(i) and log(ν) is shown in Figure 2b. The b values of peaks C1, C2, A1, and A2 are 0.758, 1.123, 0.731, and 0.749, respectively, which implies that the electrochemical reactions are mainly controlled by the pseudocapacitive behavior, and fast ionic conduction and good rate performance can be expected.[33]

Besides, the GITT measurement has been executed to calculate the Na^+ ion diffusion rate in $Cu_{2-x}Se$ electrodes. The $Cu_{2-x}Se$/Na battery was discharged at a constant current flux of 0.1 C (12 mA g^{-1}) for 600 s (τ), followed by an open circuit standing of 1 h. The GITT curve of the $Cu_{2-x}Se$/Na battery during the initial discharge process is displayed in Figure 2c, showing two distinct voltage plateaus, which are consistent with the CV curve and galvanostatic charge−discharge curve. Na^+ ion diffusion coefficients (D_{Na}) can be calculated according to the following equation:

$$D_{Na} = \frac{4}{\pi\tau}\left(\frac{m_B V_m}{M_B A}\right)^2\left(\frac{\Delta E_S}{\Delta E_\tau}\right)^2\left(\tau \ll \frac{L^2}{D_{Na}}\right) \tag{3}$$

where m_B and M_B are the mass and relative molecular weight of $Cu_{2-x}Se$, respectively, V_m is the molar volume of $Cu_{2-x}Se$, A is the electrode surface area, L is the thickness of the $Cu_{2-x}Se$ electrode, ΔE_S is the variation of steady-state voltage, and ΔE_τ is the voltage change through a discharge pulse, excluding iR drop.[8,36] The calculated D_{Na} values of the $Cu_{2-x}Se$/Na battery at different discharge states are presented in Figure 2d, which range from 3.27×10^{-13} to 7.22×10^{-10} cm^2 s^{-1}, confirming a high Na^+ ion diffusion rate in the $Cu_{2-x}Se$ electrode.[31]

Figure 2e,f shows the Nyquist plots of the $Cu_{2-x}Se$/Na battery before electrochemical test and after 20 cycles. The pristine $Cu_{2-x}Se$/Na battery shows a larger resistance, whereas the resistance reduces remarkably after 20 cycles. The impedance parameters are presented in Table 1, where R_s refers to the Ohmic resistance of the battery and R_{ct} represents the charge-transfer resistance of the battery. R_{ct} of the battery dramatically dropped to 72.6 Ω after 20 cycles, indicating the activation of the $Cu_{2-x}Se$ electrode and faster charge-transfer rate of the electrode.

Table 1. Impedance Parameters of the $Cu_{2-x}Se$/Na Battery before Cycling and after 20 Cycles

	before cycling	after 20 cycles
R_s (Ω)	10.1	13.0
R_{ct} (Ω)	742.2	72.6

Electrochemical Reaction Mechanism. To further deepen the comprehension in the electrochemical reaction mechanism of the $Cu_{2-x}Se$/Na battery, ex situ XRD was performed to explore the changes of the material structure at different charge/discharge states (Figure 3). The diffraction line of the (220) plane (44.60°, 2θ) shifts to a lower angle (44.48°) when discharged to 1.0 V and gets back to a higher angle after charged to 3.0 V (44.59°), suggesting the extraordinary structure stability of the $Cu_{2-x}Se$ material during the electrochemical process (Figure 3b). The reduced diffraction angle means that the lattice spacing of $Cu_{2-x}Se$ increases according to Bragg's law ($2d \sin\theta = n\lambda$), which can be attributed to the insertion of Na^+ ions. Generally, electrochemical reactions of transition-metal chalcogenides are based on conversion mechanism.[19,37,38] However, for some metal chalcogenides, the electrochemical mechanism is based on intercalation−conversion mechanism: the active material would first react with Na^+ ions to form an intermediate Na_xMX (M = metal and X = S or Se), and then the intermediate react with Na^+ ions subsequently.[16] $Cu_{2-x}Se$ meets the latter case; metallic Cu and Na_2Se are finally formed when the $Cu_{2-x}Se$/Na battery is discharged to 0.1 V (Figure S9), whereas there are only diffraction lines of $Cu_{2-x}Se$ when the discharge voltage is set to 1.0 V (Figure 3). There is only intercalation reaction in the $Cu_{2-x}Se$ electrode when the cutoff voltage is 1.0−3.0 V. It can be concluded that $Cu_{2-x}Se$ will maintain its stable crystal structure and suffer from less volume change during the charge−discharge process compared with materials based on the conversion mechanism (Table 2).[17,39] Ex situ XRD patterns of $Cu_{2-x}Se$ electrodes at different charge−discharge states during the 50th cycle are demonstrated in Figure S10. It can be observed that the XRD patterns change slightly compared with those of the pristine $Cu_{2-x}Se$ electrode. As indicated in the enlarged figure, the diffraction lines during the 50th cycle shift to lower degree compared with those of the pristine electrode. According to Bragg's law ($2d \sin\theta = n\lambda$), lower diffraction degree stands for larger lattice fringe. Hence, the crystal cells of $Cu_{2-x}Se$ after 50 cycles expand a little, yet the overall structure is well-maintained. It can also be observed that when the $Cu_{2-x}Se$ electrode is discharged during the 50th cycle, the diffraction line shifts to lower degree. We suppose that the electrochemical reactions are still based on the intercalation of Na^+ ions in the crystal cells of $Cu_{2-x}Se$.

Theoretical calculation was implemented to simulate the intercalation of Na^+ ions. The crystal structure of $Cu_{2-x}Se$ is displayed in Figure 4, where site a represents the vacancies in body-centered positions of $Cu_{2-x}Se$ cells and site b stands for defects of Cu atoms in crystal cells. As shown in Table 2, ΔG is −844.4 kJ mol^{-1} when Na^+ ion is inserted into site a, whereas ΔG is −229.6 kJ mol^{-1} when Na^+ ion is inserted into site b. When sites a and b are both occupied by Na^+ ions at the same time, ΔG is −17.0 kJ mol^{-1}, indicating that Na^+ ions can be inserted into these two sites theoretically. When sites a and b are occupied by Na^+ ions, the volume changes are only 16.3 and

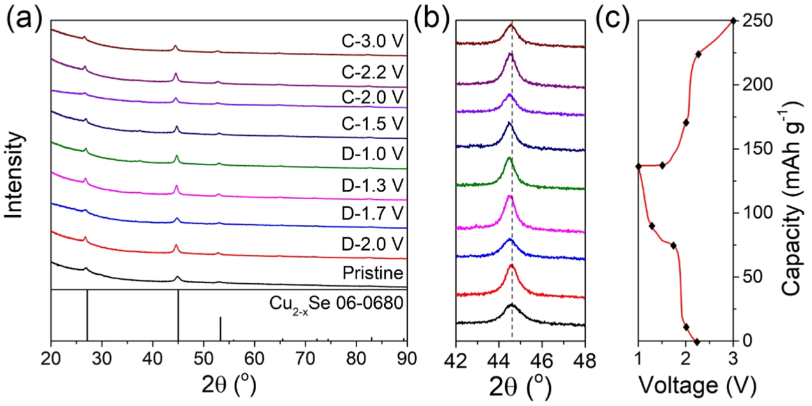

Figure 3. (a) Ex situ XRD patterns of $Cu_{2-x}Se$ electrodes in different states of charge during the initial cycle. (b) Enlarged image of the (220) plane of $Cu_{2-x}Se$ electrodes at different charge−discharge states. (c) Discharge−charge profile of the $Cu_{2-x}Se$/Na battery during the initial cycle at a current density of 50 mA g^{-1}.

Table 2. Change of Gibbs Free Energy and Cell Volume When Na^+ Ions Are Inserted into Different Sites of the $Cu_{2-x}Se$ Crystal Cell

insertion site	ΔG (kJ mol^{-1})	volume change (%)
a	−844.4	16.3
b	−229.6	9.0
a & *b*	−17.0	22.7

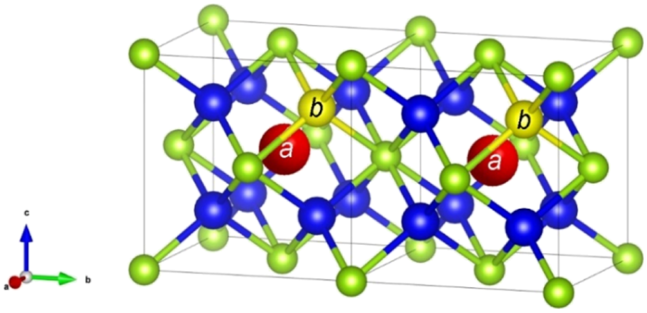

Figure 4. Crystal structure of $Cu_{2-x}Se$ and sketch of sites *a* and *b* in the crystal cells.

9.0%, respectively. Even though both sites are occupied by Na^+ ions, the volume change is still limited at 22.7%, which is a rather low level. However, the volume change of electrode materials based on conversion mechanism is usually larger. In the case of $Cu_{2-x}Se$, the cell volume is 195.3 Å^3, whereas the cell volume of Na_2Se is up to 321.8 Å^3. Therefore, the volume change will be more than 60% if $Cu_{2-x}Se$ is converted into metallic Cu and Na_2Se. Besides, conversion reaction ($MX + Na \leftrightarrow M + Na_2X$) involves phase separation of metallic metal and Na_2S/Na_2Se, which is usually harmful for the cyclic stability of active materials.

The XPS spectra of $Cu_{2-x}Se$ electrodes at different charge−discharge states were obtained to research more into the electrochemical reaction process. The XPS survey spectrum of the pristine $Cu_{2-x}Se$ electrode is illustrated in Figure 5a; peaks that belong to Cu 2p, Cu LMM, Se LMM, and Se 3d can be clearly observed. The Cu 2p XPS spectrum of the pristine $Cu_{2-x}Se$ electrode is shown in Figure 5b; two apparent peaks at 932.2 and 952.2 eV can be assigned to Cu $2p_{3/2}$ and Cu $2p_{1/2}$, respectively. A weak satellite peak at around 943.0 eV lies between these two peaks, demonstrating that the copper element is mainly in the Cu^+ state.[28,40] When discharged to 1.0 V, the peaks of Cu $2p_{3/2}$ and Cu $2p_{1/2}$ are located at 931.3 and 951.2 eV, respectively (Figure 5c). The satellite peak disappears after the initial discharge process. The reduced binding energy and the disappearance of the satellite peak represent the reduction of Cu^+ to Cu^0 when Na^+ ions are inserted into the crystal structure of $Cu_{2-x}Se$.[41] After charged to 3.0 V, the binding energies of Cu $2p_{3/2}$ and Cu $2p_{1/2}$ peaks bounce back to 932.2 and 952.2 eV, respectively, and the satellite peak reappears, indicating higher Cu valence and the extraction of Na^+ ions (Figure 5d). The XPS spectra indicate that Na^+ ions are inserted into the $Cu_{2-x}Se$ cells after discharge and the $Cu_{2-x}Se$ electrodes manifest superior reversibility during the charge−discharge process. Ex situ Raman spectra can also support our assumption, which are shown in Figure S11.

$Cu_{2-x}Se$ electrodes at different charge−discharge states were characterized by TEM tests to acquire information on the changes of morphology during the electrochemical process. Figure 6a shows the TEM image of the pristine $Cu_{2-x}Se$ electrode, and rodlike particles can be observed. The high-resolution TEM (HRTEM) image and selected area electron diffraction (SAED) pattern (inset) in Figure 6b reveal the crystalline structure of $Cu_{2-x}Se$ rods, and the lattice fringe spacing is calculated to be 0.33 nm, in accordance with the (111) plane of cubic $Cu_{2-x}Se$. Figure 6c,d exhibits the TEM images of the $Cu_{2-x}Se$ electrode discharged to 1.0 V, and Figure 6e,f shows the TEM images of the $Cu_{2-x}Se$ electrode charged to 3.0 V. The morphology of the $Cu_{2-x}Se$ nanorods is well-maintained after the initial discharge−charge process, and the SAED patterns also have no significant change. No Na_2Se, metallic Cu, or intermediates can be observed, supporting the assumption that only intercalation/deintercalation reactions happen during the electrochemical process. In summary, the one-dimensional morphology of $Cu_{2-x}Se$ is well-maintained and lattice fringe remains unchanged during the initial discharge−charge process, demonstrating the stable structure of $Cu_{2-x}Se$ during the intercalation/deintercalation of Na^+ ions.

■ CONCLUSIONS

In summary, one-dimensional $Cu_{2-x}Se$ nanorods are synthesized by a water evaporation approach. The as-prepared $Cu_{2-x}Se$ rods show a uniform morphology with a diameter of 300−800 nm and a length up to dozens of micrometers. By adjusting the discharge−charge voltage range to 1.0−3.0 V, the electrochemical reaction process of $Cu_{2-x}Se$/Na batteries is

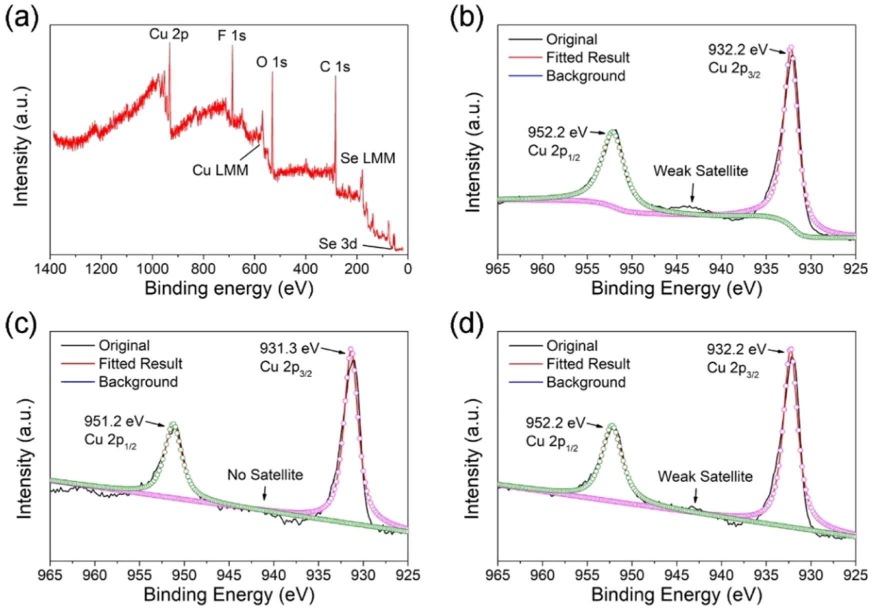

Figure 5. (a) XPS survey spectrum of the pristine $Cu_{2-x}Se$ electrode; (b) XPS Cu 2p spectrum of the pristine $Cu_{2-x}Se$ electrode; (c) XPS Cu 2p spectrum of the $Cu_{2-x}Se$ electrode discharged to 1.0 V; and (d) XPS Cu 2p spectrum of the $Cu_{2-x}Se$ electrode charged to 3.0 V.

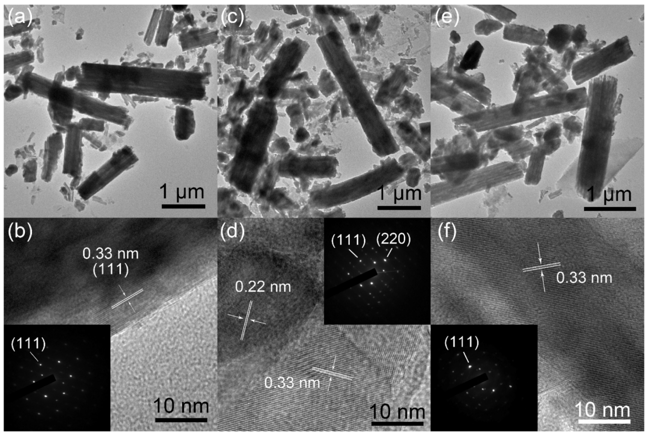

Figure 6. (a) TEM image, (b) HRTEM image, and SAED pattern (inset) of the pristine $Cu_{2-x}Se$ electrode; (c) TEM image, (d) HRTEM image, and SAED pattern (inset) of the $Cu_{2-x}Se$ electrode discharged to 1.0 V; and (e) TEM image, (f) HRTEM image, and SAED pattern (inset) of the $Cu_{2-x}Se$ electrode charged to 3.0 V.

mainly an intercalation/deintercalation reaction, leading to the outstanding cyclic stability. After 400 cycles at a current density of 100 mA g^{-1}, the discharge capacity of the $Cu_{2-x}Se$ electrode remains at 106.2 mA h g^{-1} and the capacity retention rate is up to 83.0%. $Cu_{2-x}Se$/Na batteries also show good rate performance, and the discharge capacities of the $Cu_{2-x}Se$ electrode are 124.7, 111.4, 102.2, 88.5, 75.9, 65.2, and 62.8 mA h g^{-1} at current densities of 50, 100, 200, 400, 800, 1600, and 2000 mA g^{-1}, respectively. CV and GITT tests indicate the pseudocapacitive behavior and fast Na^+ ion diffusion rate of the $Cu_{2-x}Se$ electrode. Ex situ XRD patterns demonstrate the insertion/extraction process of Na^+ ions. TEM tests, XPS spectra, and Raman spectra of $Cu_{2-x}Se$ electrodes at different electrochemical states also reveal the reversible insertion/extraction of Na^+ ions and stable crystal structure of $Cu_{2-x}Se$. $Cu_{2-x}Se$ can be a favorable electrode material for NIBs, and this work can deepen the understanding of the electrochemical reaction mechanism occurred in NIBs.

■ EXPERIMENTAL PROCEDURES

Raw Materials and Synthesis. Selenium powder (≥99.99%, metal basis), water-free $NaClO_4$ (99.99%), and sodium metal (99.7%) were obtained from Shanghai Aladdin Bio-Chem Technology Co., Ltd. NaOH (analytical reagent, AR) and $Cu(NO_3)_2$ (AR) were purchased from Shanghai Chemical Co., Ltd. Acetylene black, polyvinylidene fluoride (PVDF), *N*-methylpyrrolidone (NMP), and triethylene glycol dimethyl ether (TEGDME) were all of battery grade. All chemical reagents were not further purified.

$Cu_{2-x}Se$ nanorods were prepared by a water evaporation method. In a typical synthesis process, 5.0 g of NaOH, 0.15 g of selenium powder, and 20 mL of deionized water were added into a beaker, and then the beaker was heated to 80 °C under magnetic stirring. Selenium powder was gradually dissolved, and a deep red solution was obtained after a few minutes. Black precipitation was instantly formed after adding 1.5 mL of $Cu(NO_3)_2$ aqueous solution (0.5 mol L^{-1}) into the solution. Subsequently, the beaker was placed in a 140 °C fan-forced oven for 5 h. Solid substance in the beaker was washed with hot water and dehydrated ethanol several times. Black powders were collected eventually after vacuum dehydration.

Characterization. A Rigaku Ultima IV diffractometer (Rigaku Corporation, Japan) was used to record XRD patterns at 40 kV and 30 mA with Cu $K\alpha$ radiation. Raman spectra were acquired using a Renishaw confocal Raman microscope (Renishaw plc., UK). The laser wavelength was 532 nm, and the laser power was set to 10 μW. Field-emission SEM images were taken on Hitachi S-4800 (Hitachi Corporation, Japan) with EDS. TEM images and SAED patterns were obtained from JEM-2100 (JEOL, Japan) at an accelerating voltage of 200 kV, whereas high-angle annular dark field (HAADF) images and EDS mapping were acquired from Tecnai F30 (FEI, US) at an accelerating voltage of 300 kV. XPS spectra were measured using a PHI Quantum 2000 scanning ESCA microprobe with Al $K\alpha$ radiation (Physical Electronics Inc., US). For ex situ XRD, TEM, XPS, and Raman tests, batteries at different charge−discharge states were dismantled and $Cu_{2-x}Se$ electrodes were collected and washed with the electrolyte solvent (TEGDME) to remove residual sodium salt. The as-prepared electrodes were used for ex situ tests.

Electrochemical Tests. The electrochemical characterizations were performed with CR2032 coin cells. $Cu_{2-x}Se$ nanorods, acetylene black, and PVDF were mixed with a weight ratio of 80:10:10 in NMP. The slurry was overlaid on copper foils and placed in a vacuum drying oven (60 °C) to remove residual NMP. Then, the electrode sheet was punched into round discs with a diameter of 12 mm. The loading mass of active material is around 1.84−2.40 mg per electrode (1.63−2.12 mg cm^{-2}). $Cu_{2-x}Se$/Na batteries were assembled in an argon-filled glovebox (Mbraun, Germany). The $Cu_{2-x}Se$ electrode was the positive electrode, and sodium metal was used as the negative electrode. The electrolyte was 1 mol L^{-1} $NaClO_4$ dissolved in TEGDME. The separator used in the battery was Celgard 2400 (Celgard, LLC., US). CHI 1030C multipotentiostat (Shanghai Chenhua Electrochemical Instruments, P. R. China) was selected to perform CV tests. A Neware CT-3008W battery testing system (Neware Technology Ltd., P. R. China) was used to carry out galvanostatic charge−discharge tests and GITT tests. EIS was performed on a Solartron 1260A and 1287A impedance/gain-phase Analyzer (AMETEK, UK). All electrochemical tests were performed at room temperature (25 °C).

Calculation Procedure. The Gaussian 09 computational package was used to perform the theoretical calculation. Geometries of all structures were fully optimized at the B3PW91 level of density functional theory. The LanL2DZ basis set was employed for Se atoms, and the 6-311G basis set was used to describe H, C, and O atoms.

■ ASSOCIATED CONTENT

Ⓢ Supporting Information

The Supporting Information is available free of charge on the ACS Publications website at DOI: 10.1021/acsami.8b00783.

Growth of $Cu_{2-x}Se$ nanorods, XRD pattern, Raman spectrum, SEM and TEM images, EDS spectrum of the as-prepared $Cu_{2-x}Se$ nanorods, optimization of cutoff voltage of the $Cu_{2-x}Se$ electrodes, XRD pattern of the $Cu_{2-x}Se$ electrode discharged to 0.1 V, ex situ XRD patterns of the $Cu_{2-x}Se$ electrodes during the 50th cycle, ex situ Raman spectra of the $Cu_{2-x}Se$ electrodes at different charge−discharge states, and HAADF image and EDS mapping images of $Cu_{2-x}Se$ discharged to 1.0 V (PDF)

■ AUTHOR INFORMATION

Corresponding Author

*E-mail: jbzhao@xmu.edu.cn.

ORCID

He Li: 0000-0002-5324-8101
Bing-Joe Hwang: 0000-0002-3873-2149
Jinbao Zhao: 0000-0002-2753-7508

Author Contributions

[§]H.L. and J.J. contributed equally to this work and share the first authorship.

Notes

The authors declare no competing financial interest.

■ ACKNOWLEDGMENTS

The authors acknowledge financial support from the National Natural Science Foundation of China (grants nos. 21273185 and 21621091). They appreciate Dr. Binbin Xu and Qiming Hong of Xiamen University for their assistance in TEM tests. Special acknowledgement is delivered to Prof. Daiwei Liao of Xiamen University for his careful reading and corrections.

■ REFERENCES

(1) Goodenough, J. B.; Kim, Y. Challenges for Rechargeable Li Batteries. *Chem. Mater.* **2010**, *22*, 587−603.

(2) Etacheri, V.; Marom, R.; Elazari, R.; Salitra, G.; Aurbach, D. Challenges in the Development of Advanced Li-Ion Batteries: a Review. *Energy Environ. Sci.* **2011**, *4*, 3243−3262.

(3) Tarascon, J.-M. Is Lithium the New Gold? *Nat. Chem.* **2010**, *2*, 510.

(4) Dahbi, M.; Yabuuchi, N.; Kubota, K.; Tokiwa, K.; Komaba, S. Negative Electrodes for Na-Ion Batteries. *Phys. Chem. Chem. Phys.* **2014**, *16*, 15007−15028.

(5) You, Y.; Yao, H.-R.; Xin, S.; Yin, Y.-X.; Zuo, T.-T.; Yang, C.-P.; Guo, Y.-G.; Cui, Y.; Wan, L.-J.; Goodenough, J. B. Subzero-Temperature Cathode for a Sodium-Ion Battery. *Adv. Mater.* **2016**, *28*, 7243−7248.

(6) Zhang, C.; Xu, Y.; Zhou, M.; Liang, L.; Dong, H.; Wu, M.; Yang, Y.; Lei, Y. Potassium Prussian Blue Nanoparticles: A Low-Cost Cathode Material for Potassium-Ion Batteries. *Adv. Funct. Mater.* **2017**, *27*, 1604307.

(7) Zeng, J.; Yang, Y.; Li, C.; Li, J.; Huang, J.; Wang, J.; Zhao, J. Li_3VO_4: an Insertion Anode Material for Magnesium Ion Batteries with High Specific Capacity. *Electrochim. Acta* **2017**, *247*, 265−270.

(8) Jiang, J.; Li, H.; Huang, J.; Li, K.; Zeng, J.; Yang, Y.; Li, J.; Wang, Y.; Wang, J.; Zhao, J. Investigation of the Reversible Intercalation/Deintercalation of Al into the Novel Li_3VO_4@C Microsphere Composite Cathode Material for Aluminum-Ion Batteries. *ACS Appl. Mater. Interfaces* **2017**, *9*, 28486−28494.

(9) Yabuuchi, N.; Kubota, K.; Dahbi, M.; Komaba, S. Research Development on Sodium-Ion Batteries. *Chem. Rev.* **2014**, *114*, 11636−11682.

(10) Hwang, J.-Y.; Myung, S.-T.; Sun, Y.-K. Sodium-Ion Batteries: Present and Future. *Chem. Soc. Rev.* **2017**, *46*, 3529−3614.

(11) Kim, H.; Kim, H.; Ding, Z.; Lee, M. H.; Lim, K.; Yoon, G.; Kang, K. Recent Progress in Electrode Materials for Sodium-Ion Batteries. *Adv. Energy Mater.* **2016**, *6*, 1600943.

(12) Yan, Y.; Yin, Y.-X.; Guo, Y.-G.; Wan, L.-J. A Sandwich-Like Hierarchically Porous Carbon/Graphene Composite as a High-Performance Anode Material for Sodium-Ion Batteries. *Adv. Energy Mater.* **2014**, *4*, 1301584.

(13) Hou, H.; Qiu, X.; Wei, W.; Zhang, Y.; Ji, X. Carbon Anode Materials for Advanced Sodium-Ion Batteries. *Adv. Energy Mater.* **2017**, *7*, 1602898.

(14) Stevens, D.; Dahn, J. High Capacity Anode Materials for Rechargeable Sodium-Ion Batteries. *J. Electrochem. Soc.* **2000**, *147*, 1271−1273.

(15) Yu, L.; Wang, L. P.; Xi, S.; Yang, P.; Du, Y.; Srinivasan, M.; Xu, Z. J. β-FeOOH: An Earth-Abundant High-Capacity Negative Electrode Material for Sodium-Ion Batteries. *Chem. Mater.* **2015**, *27*, 5340−5348.

(16) Xiao, Y.; Lee, S. H.; Sun, Y.-K. The Application of Metal Sulfides in Sodium Ion Batteries. *Adv. Energy Mater.* **2016**, *7*, 1601329.

(17) Hu, Z.; Zhu, Z.; Cheng, F.; Zhang, K.; Wang, J.; Chen, C.; Chen, J. Pyrite FeS_2 for High-Rate and Long-Life Rechargeable Sodium Batteries. *Energy Environ. Sci.* **2015**, *8*, 1309−1316.

(18) Zhang, F.; Xia, C.; Zhu, J.; Ahmed, B.; Liang, H.; Velusamy, D. B.; Schwingenschlögl, U.; Alshareef, H. N. $SnSe_2$ 2D Anodes for Advanced Sodium Ion Batteries. *Adv. Energy Mater.* **2016**, *6*, 1601188.

(19) Hu, Z.; Liu, Q.; Chou, S.-L.; Dou, S.-X. Advances and Challenges in Metal Sulfides/Selenides for Next-Generation Rechargeable Sodium-Ion Batteries. *Adv. Mater.* **2017**, *29*, 1700606.

(20) Li, H.; Wang, Y.; Huang, J.; Zhang, Y.; Zhao, J. Microwave-Assisted Synthesis of CuS/Graphene Composite for Enhanced Lithium Storage Properties. *Electrochim. Acta* **2017**, *225*, 443−451.

(21) Wang, Y.; Zhang, Y.; Li, H.; Peng, Y.; Li, J.; Wang, J.; Hwang, B.-J.; Zhao, J. Preparation of One-Dimensional Bamboo-Like $Cu_{2-x}S$@C Nanorods with Enhanced Lithium Storage Properties. *Electrochim. Acta* **2017**, *247*, 271−280.

(22) Yue, J.-L.; Sun, Q.; Fu, Z.-W. Cu_2Se with Facile Synthesis as a Cathode Material for Rechargeable Sodium Batteries. *Chem. Commun.* **2013**, *49*, 5868−5870.

(23) Pan, Z.-Z.; Yan, Y.; Cui, N.; Xie, J.-C.; Zhang, Y.-B.; Mu, W.-S.; Hao, C. Ionic Liquid-Assisted Preparation of Sb_2S_3/Reduced Graphene Oxide Nanocomposite for Sodium-Ion Batteries. *Adv. Mater. Interfaces* **2018**, *5*, 1701481.

(24) Liu, H.; Shi, X.; Xu, F.; Zhang, L.; Zhang, W.; Chen, L.; Li, Q.; Uher, C.; Day, T.; Snyder, G. J. Copper Ion Liquid-Like Thermoelectrics. *Nat. Mater.* **2012**, *11*, 422−425.

(25) Chen, D.; Chen, G.; Jin, R.; Xu, H. Self-Decorated $Cu_{2-x}Se$ Nanosheets as Anode Materials for Li Ion Batteries and Electrochemical Hydrogen Storage. *CrystEngComm* **2014**, *16*, 2810−2817.

(26) Li, X.; He, X.; Shi, C.; Liu, B.; Zhang, Y.; Wu, S.; Zhu, Z.; Zhao, J. Synthesis of One-Dimensional Copper Sulfide Nanorods as High-Performance Anode in Lithium Ion Batteries. *ChemSusChem* **2014**, *7*, 3328−3333.

(27) Xu, J.; Zhang, W.; Yang, Z.; Ding, S.; Zeng, C.; Chen, L.; Wang, Q.; Yang, S. Large-Scale Synthesis of Long Crystalline $Cu_{2-x}Se$ Nanowire Bundles by Water-Evaporation-Induced Self-Assembly and Their Application in Gas Sensing. *Adv. Funct. Mater.* **2009**, *19*, 1759−1766.

(28) Li, H.; Jiang, J.; Wang, F.; Huang, J.; Wang, Y.; Zhang, Y.; Zhao, J. Facile Synthesis of Rod-like $Cu_{2-x}Se$ and Insight into Its Improved Lithium-Storage Property. *ChemSusChem* **2017**, *10*, 2235−2241.

(29) Minceva-Sukarova, B.; Najdoski, M.; Grozdanov, I.; Chunnilall, C. J. Raman Spectra of Thin Solid Films of Some Metal Sulfides. *J. Mol. Struct.* **1997**, *410−411*, 267−270.

(30) Filippo, E.; Manno, D.; Serra, A. Synthesis and Growth Mechanism of Dendritic $Cu_{2-x}Se$ Microstructures. *J. Alloys Compd.* **2012**, *538*, 8−10.

(31) Li, H.; Wang, Y.; Jiang, J.; Zhang, Y.; Peng, Y.; Zhao, J. CuS Microspheres as High-Performance Anode Material for Na-Ion Batteries. *Electrochim. Acta* **2017**, *247*, 851−859.

(32) Ko, Y. N.; Kang, Y. C. Co_9S_8-Carbon Composite as Anode Materials with Improved Na-Storage Performance. *Carbon* **2015**, *94*, 85−90.

(33) Zhang, K.; Hu, Z.; Liu, X.; Tao, Z.; Chen, J. $FeSe_2$ Microspheres as a High-Performance Anode Material for Na-Ion Batteries. *Adv. Mater.* **2015**, *27*, 3305−3309.

(34) Zhang, K.; Park, M.; Zhou, L.; Lee, G.-H.; Li, W.; Kang, Y.-M.; Chen, J. Urchin-Like $CoSe_2$ as a High-Performance Anode Material for Sodium-Ion Batteries. *Adv. Funct. Mater.* **2016**, *26*, 6728−6735.

(35) Shen, L.; Lv, H.; Chen, S.; Kopold, P.; van Aken, P. A.; Wu, X.; Maier, J.; Yu, Y. Peapod-Like Li_3VO_4/N-Doped Carbon Nanowires with Pseudocapacitive Properties as Advanced Materials for High-Energy Lithium-Ion Capacitors. *Adv. Mater.* **2017**, *29*, 1700142.

(36) Shaju, K. M.; Rao, G. V. S.; Chowdari, B. V. R. Influence of Li-Ion Kinetics in the Cathodic Performance of Layered Li$(Ni_{1/3}Co_{1/3}Mn_{1/3})O_2$. *J. Electrochem. Soc.* **2004**, *151*, A1324.

(37) Klein, F.; Jache, B.; Bhide, A.; Adelhelm, P. Conversion Reactions for Sodium-Ion Batteries. *Phys. Chem. Chem. Phys.* **2013**, *15*, 15876−15887.

(38) Su, Q.; Du, G.; Zhang, J.; Zhong, Y.; Xu, B.; Yang, Y.; Neupane, S.; Li, W. *In Situ* Transmission Electron Microscopy Observation of Electrochemical Sodiation of Individual Co_9S_8-Filled Carbon Nanotubes. *ACS Nano* **2014**, *8*, 3620−3627.

(39) Hu, Z.; Wang, L.; Zhang, K.; Wang, J.; Cheng, F.; Tao, Z.; Chen, J. MoS_2 Nanoflowers with Expanded Interlayers as High-Performance Anodes for Sodium-Ion Batteries. *Angew. Chem.* **2014**, *126*, 13008−13012.

(40) Deroubaix, G.; Marcus, P. X-Ray Photoelectron Spectroscopy Analysis of Copper and Zinc Oxides and Sulphides. *Surf. Interface Anal.* **1992**, *18*, 39−46.

(41) Liu, C.; Xian, H.; Jiang, Z.; Wang, L.; Zhang, J.; Zheng, L.; Tan, Y.; Li, X. Insight into the Improvement Effect of the Ce Doping into the SnO_2 Catalyst for the Catalytic Combustion of Methane. *Appl. Catal., B* **2015**, *176−177*, 542−552.